技 術 論 文

Analysis of Cycle-to-Cycle Variation in a Port Injection Gasoline Engine by Simultaneous Measurement of Time Resolved PIV and PLIF

Santa Haramiishi   Takahiro Watanabe   Minoru Iida   Satoshi Hokimoto
Tatsuya Kuboyama   Yasuo Moriyoshi

要旨

　低負荷運転時における燃焼のサイクル変動は、エンジンの運転に様々な問題を引き起こす要因となる。この変動を低減するために可変バルブタイミングや可変点火タイミングなどの手法が用いられる。しかし、これらの手法は搭載性やコストの問題から二輪車用エンジンへ積極的に採用されることは少ない。そのため、複雑な機構や電子制御を用いることなく、燃焼サイクル変動を抑えたエンジンの開発が求められている。燃焼のサイクル変動は、筒内流動、空燃比、温度、残留ガス、点火エネルギなどの変動によって引き起こされると考えられる。本研究では、燃焼サイクル変動と筒内流動の変動、および燃料濃度の変動との関係に着目した。筒内流動の変動を評価するために、高時間分解粒子画像流速測定法（TR-PIV）を用いた。さらに、燃料濃度の空間分布を計測するために、平面レーザー誘起蛍光法（PLIF）を用いた。これら二つの可視化技術を同時に用いて、連続燃焼サイクルを計測した。計測の結果、図示平均有効圧の変動は、乱流運動エネルギと燃料濃度の変動によって説明することができた。多くのサイクルでは、図示平均有効圧と乱流運動エネルギとの間で相関を確認することができた。また残りのサイクルでは、図示平均有効圧と燃料濃度の間で相関が確認できた。今後、図示平均有効圧に対する各要素の寄与度を考察する。また、乱流運動エネルギの変動はタンブル渦構造の変動によって引き起こされることが著者らの先行研究で確認されている[2][13]。

Abstract

Cycle-to-cycle variation (CCV) of combustion in low load operation is a factor that may cause various problems in engine operation. Variable valve timing and variable ignition timing are commonly used as a means to reduce this variation. However, due to mountability and cost constraints, these methods are not feasible for use in motorcycle engines. Therefore, development of an engine with minimal CCV without utilizing complicated mechanisms or electronic control is required. CCV of combustion may be caused by fluctuations in in-cylinder flow, air-fuel mixture, temperature, residual gas and ignition energy. In this study, the relationship between CCV of combustion, in-cylinder flow fluctuation and air-fuel mixture fluctuation was the primary focus. In order to evaluate in-cylinder flow fluctuation, Time Resolved Particle Image Velocimetry (TR-PIV) technique was utilized. In addition, Planar Laser Induced Fluorescence (PLIF) technique was used to measure spatial distribution of the mixture. These two visualization techniques were used together to measure continuous combustion cycles. The fluctuation of net IMEP can be explained by the fluctuation of Turbulence Kinetic Energy (TKE) and fuel concentration. In most cycles, net IMEP was correlated with TKE. In the remaining cycles, net IMEP was correlated with fuel concentration. The contribution of each factor towards net IMEP is to be discussed. It has been also confirmed that TKE fluctuation is caused by fluctuation in the tumble vortex structure, as shown in the authors' previous study[2][13].

1 INTRODUCTION

CCV of combustion not only limits the potential of the output power characteristics but also causes various problems such as a decrease in thermal efficiency and deterioration of exhaust gas quality. Many pieces of

research have been conducted to reduce CCV of combustion. In particular, for a four-wheeled vehicle engine, the combustion fluctuation can be reduced by optimizing ignition system, fuel injection system and valve control system. To do so, many complicated mechanisms and electronic control systems are used. However, for a motorcycle engine, it is not feasible to use such complicated solutions due to mountability and cost constraints. Therefore, development of an engine with minimal CCV without utilizing complicated mechanisms or electronic control is required. Most motorcycles are targeted more towards the enthusiast market segment, as a result of which their engines are required to have high output power characteristics. These engines are usually not suited for low load operation, as they are optimized for operation under high load and high revolution speed conditions. Valve overlap optimized for high load operation often causes problems with high residual gas accumulation in low load operation, and worsens CCV of combustion. Also, the throttle valve usually has a large diameter in order to obtain a high maximum output power, which leads to a lack of controllability of the air flow into the cylinder in low load conditions. In some cases, the ignition timing is retarded to prevent a sharp rise in engine torque. This ignition timing retardation worsens CCV of combustion.

CCV of combustion depends on various elements in the cylinder at the ignition timing. CCV of combustion may be caused by fluctuations in in-cylinder flow, air-fuel mixture, temperature, residual gas and ignition energy. As these factors fluctuate from cycle to cycle, the conditions near the spark plug change, and that induces fluctuations in the initial flame growth. As a result, fluctuations in net IMEP occur. Several studies in the past have utilized flow visualization experiments to analyze combustion cyclic fluctuation. Müller et al. focused on the cyclic fluctuation of tumble vortex structure under motoring conditions. They reported that the position of the tumble vortices can fluctuate greatly in the horizontal direction, and that the kinetic energy and the turbulence kinetic energy history are affected significantly by variation in the vortex structure[1]. Furthermore, in this author's previous study,

it was confirmed that the cyclic fluctuation of intake flow increases as the engine operation load decreases under motoring conditions[2]. Sholes et al. confirmed that the cyclic fluctuation is suppressed under strong tumble flow condition[3]. Cyclic fluctuation of in-cylinder flow also affects spray shape. Zeng et al. experimentally confirmed that the spray shape changes due to cyclic fluctuation of in-cylinder flow before fuel injection in a direct fuel injection (DI) gasoline engine[4]. As an example of research on the firing conditions, Fontanesi et al. analyzed the effect of the spark plug ground electrode orientation on the local flow and on the cyclic fluctuation of the flame propagation pattern using LES (Large eddy simulation)[5]. Furthermore, as an example of experimental study of a DI gasoline engine, Peterson et al. conducted two studies, the first of which analyzed combustion cyclic fluctuation from simultaneous measurement of local flow and fuel concentration distribution, and the second evaluated ignition energy and initial flame growth[6][7].

Although many studies about combustion cyclic fluctuation have been conducted, there are very few examples of analyses performed under low load firing and port fuel injection (PFI) conditions, where fuel concentration stratification is less likely to occur compared to direct fuel injection conditions. In this study, using PFI single-cylinder visualization engine, simultaneous measurement of flow field and mixture distribution under low load firing condition was conducted to analyze the factors that cause combustion cyclic fluctuation. TR-PIV was used to measure the flow field, and PLIF was used to measure the air-fuel mixture distribution. As described above, the cyclic fluctuation is caused by variation in various factors. In this study, the primary focus was to identify the relationship between CCV of combustion, in-cylinder flow fluctuation and air-fuel mixture fluctuation. Fluctuation in parameters other than in-cylinder flow and air-fuel mixture was minimized by optimizing the measurement conditions, and the contribution of these two parameters to CCV of combustion was analyzed.

2 EXPERIMENTAL SETUP AND ANALYTICAL METHOD

2-1. Optical Engine

The visualization single-cylinder engine (KOYAMA GARAGE) used in this study is shown in Figure 1. This visualization engine uses quartz glass for the pent roof and the cylinder liner, and thus, the entire area inside of the chamber and cylinder can be observed from the front. A quartz glass window is inserted into the piston crown. Using a light source and a mirror placed below the piston, the cylinder interior can be illuminated from underneath through this window. This visualization piston has been changed since the time of authors' previous study, and the visualization range has been expanded. Figure 2 shows the visualization piston used in this study (right) and the one used previously (left). The new visualization piston facilitates measurement of wider cross sections, as it has a width of 58 mm at the bore central cross section and 41 mm at the intake valve cross section. In this study, measurements were only taken at the central cross section. The specifications of the visualization engine is shown in Table 1. The engine head uses one cylinder from a 2-L, 4-cylinder mass-production four-wheeled vehicle engine, and the displacement per cylinder is 500 cm^3. The bore and stroke are 86×86 mm square and the compression ratio is 9.2. The timing of the intake and exhaust valves of this visualization engine can be set arbitrarily. In previous sections, it was stated that the valve overlap is wide in motorcycle engines. However, in this study, the valve timing was set so that the valve overlap would be zero in order to reduce the influence of residual gas fluctuation on CCV of combustion. The valve timing is shown in Table 1. Although this visualization engine can be installed with either PFI or DI, experiments were conducted under PFI conditions since motorcycle engines are targeted. The in-cylinder pressure was measured using a piezoelectric pressure sensor (Kistler, 6052C) installed on the chamber, and the intake and exhaust pressure was measured using absolute pressure sensors (Kistler, 4005B, 4007C) installed on the intake pipe and the exhaust pipe, respectively. These were measured at 1

degree crank angle intervals by a high-speed data logger (YOKOGAWA, DL750). The in-cylinder piezo sensor was calibrated by adjusting its absolute pressure correction setting, such that it reported pressures equal to the
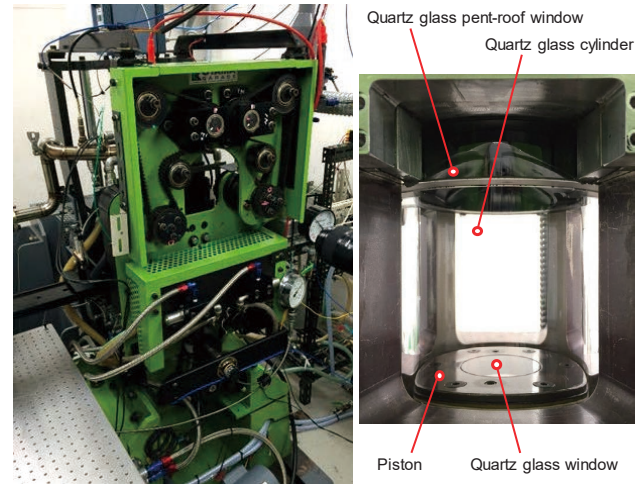

Fig. 1 Optical engine

Fig. 2 Visualization piston; Right is used in this study and left is used in previous study.

Table 1 Engine specification

Displaced volume	500 cm^3
Stroke	86 mm
Bore	86 mm
Connecting rod length	139 mm
Compression ratio	9.2:1
Number of valves	4
Intake valve open	360 deg. ATDC
Intake valve close	600 deg. ATDC
Exhaust valve open	130 deg. ATDC
Exhaust valve close	360 deg. ATDC
Injection type	PFI
Material of cylinder liner	Quartz glass

intake pressure sensor between crank angle 390 deg. and 570 deg. ATDC (After Top Dead Center). The air-fuel ratio was measured using an A/F sensor (NGK, ZFAS-U1) installed in the exhaust pipe, and the intake and exhaust temperatures were measured using a K-type sheath thermocouple. These were measured at 200 ms intervals by a low-speed data logger (OMRON, ZR-45).
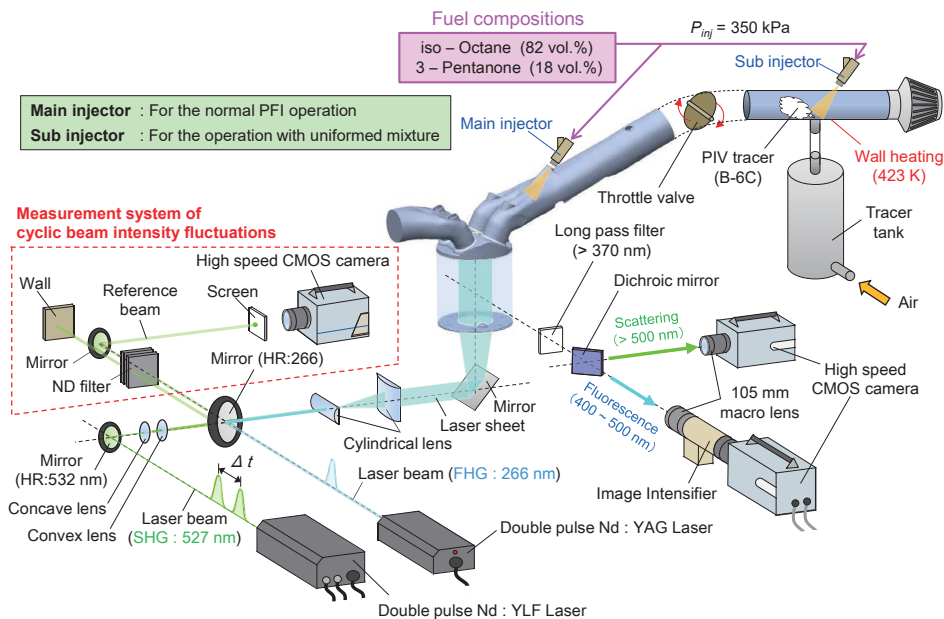
2-2. Optical Setup

A schematic diagram of the optical setup is shown in Figure 3. This optical setup is designed to simultaneously perform flow field measurement by PIV and fuel concentration distribution measurement by PLIF. The light source for PIV is a second harmonic generation of high frequency dual-cavity Nd: YLF laser (New Wave Research, Pegasus-PIV, 10 kHz, 527 nm, 4 mJ/pulse). Fourth harmonic generation of a dual-cavity Nd: YAG laser (New Wave Research, SOLO-120, 15 Hz, 266 nm, 25 mJ/pulse) is used as the light source for PLIF. The laser beams are placed on the same optical axis through a HR 266 nm mirror (SIGMAKOKI, TFMHP-266, HR 266 nm: 98%). These laser beams are formed into light sheet using two cylindrical lenses (SIGMAKOKI), and the sheet width and thickness are adjusted appropriately. These beams are irradiated into the cylinder through a mirror below the piston. PIV tracer particles suspended in the

flow, upon illumination by the Nd:YLF laser, perform Mie scattering at a wavelength of 527 nm. On the other hand, PLIF tracer emit fluorescence at wavelengths in the range of 420-450 nm when irradiated by 266 nm of the Nd:YAG laser. These two wavelength ranges are separated by a dichroic mirror (IRIDIAN, 495 DPS, HR> 500 nm: 99%, HT 400-500 nm: 96.3%) after passing through a long pass filter with a cutoff wavelength of 370 nm. After that, scattered light for PIV is reflected by the dichroic mirror and photographed by a high-speed CMOS monochrome camera (Photron, SA-X2) equipped with a macro lens (Nikon, AI AF Micro Nikkor 105 mm F 2.8 D). Fluorescent light for PLIF transmits through the dichroic mirror, and is photographed by a 16bit CMOS color camera (Photron, FASTCAM SA-X) equipped with a macro lens (Nikon, Ai AF Micro Nikkor 105 mm F 2.8 D) through an image intensifier (HAMAMATSU, C10880). In Figure 3, the part enclosed in red dashed lines shows the apparatus using which PLIF calibration data is acquired. The details are described in the "PLIF system" section.

2-3. PIV System

A schematic diagram of the measurement range is shown in Figure 4. The width of the measurement range is 58 mm, which is approximately 67% of the bore (86 mm). The specifications of the PIV system are shown in Table 2. PIV

Fig. 3 Schematic of Optical setup
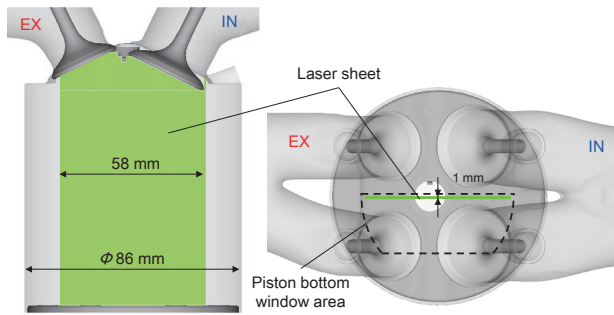
Fig. 4 Schematic of measurement range

Table 2 PIV and PLIF specifications

	PIV	PLIF
Laser types	Double pulse Nd: YLF	Double pulse Nd: YAG
Wave lengths	527 nm (SHG)	266 nm (FHG)
Sheet thickness	1 mm	1 mm
Shot timings	358 to 714 deg. ATDC	-120 and -7 deg. ATDC
Measurement intervals in a cycle	2 deg. (3 kHz)	None
Particle image intervals Δt	25 μs (Intake stroke) 50 μs (Compression stroke)	None
Frame rates	20000 fps	6000 fps
Shutter speeds	1/20416	1/6037
Spatial resolutions	672×1024 (0.8 mm/vector)	1024×1024 (0.15 mm/pix.)

measurement was performed from 358 deg. ATDC to 714 deg. ATDC, which is 1 degree before the ignition timing. The measurement interval was 2 degrees, corresponding to a measurement frequency of 3 kHz at an engine rotating speed of 1000 rpm. The oscillation timing of the Nd:YLF laser was controlled by a trigger signal synchronized with the crank angle. The synchronized signal was generated by a divider circuit and a pulse generator (nf, WAVE FACTORY WF1946) based on an angle signal from a rotary encoder (OMRON, E6B2-CWZ3E) connected to the crankshaft.

SiO$_2$ hollow porous particles (SUZUKI YUSHI KOGYO, Godball B-6C) with a diameter of about 2 ~ 5 μm were used as the PIV tracer. The tracer particles were introduced into the intake flow using compressed air upstream of the throttle valve. At a PIV measurement frequency of 3 kHz, this tracer exhibits as high as 99.3% frequency responsiveness (@ 2 μm). The flow trackability is also adequate[8].

The thickness of the PIV laser sheet was set to 1 mm based on the quarter rule, which states that particle displacement perpendicular to the measurement plane between two consecutive image captures should not be more than 1/4 of the laser sheet thickness[9]. For optimal tracking of particle trajectories, the in-plane particle displacement between two consecutive images should be 5 to 10 pixels[10]. The average flow velocity in the cylinder varies by as much as an order of magnitude between the intake and compression strokes. Therefore, if PIV analysis is performed on the entire process at a constant particle image interval Δt, the measurement accuracy is not adequate. In this study, the particle image interval Δt was chosen to be 25 μs in the intake stroke, and 50 μs in the compression stroke. This switching of particle image interval within a single cycle led to an improvement in measurement accuracy. The images were taken using frame straddling technique to synchronize the laser oscillation timing with the imaging timing of the camera.

PIV analysis was performed using commercial software DANTEC, Dynamic studio ver. 2015a. Analysis was performed using the FFT (Fast Fourier Transform) correlation method. Correlations were made using 50% overlap in three stages with each stage having a different search area (8×8, 16×16, 32×32 pixels). Erroneous vectors were removed using a median filter with a window size of 3×3 vectors. The obtained numerical data was post-processed using open source software SCILAB Enterprise, Scilab ver. 5.5.2 and C# original codes. Vector maps and contour maps were made using a post-processing commercial software i-WORKS, GraphR plus, ver.1.57.

2-4. Separation between Averaged Flow and Turbulent Component from Instantaneous Flow

In order to evaluate cyclic fluctuation of in-cylinder flow, it is necessary to separate the turbulent flow component from the instantaneous flow. The resulting average flow component represents time-averaged flow in one cycle, and therefore includes the effects of cycle to cycle flow variation. Overall the instantaneous flow velocity, $\tilde{u}$ is

defined as sum of ensemble-averaged, $\langle u \rangle$ cyclic fluctuation component, u_c and turbulent component, u' (1). Since it does not include cyclic fluctuation component, ensemble-averaged alone cannot be used to evaluate cyclic fluctuation. The ensemble-averaged flow velocity component and cycle variation component combined represent the time-averaged flow velocity component, $\bar{u}$ (2).
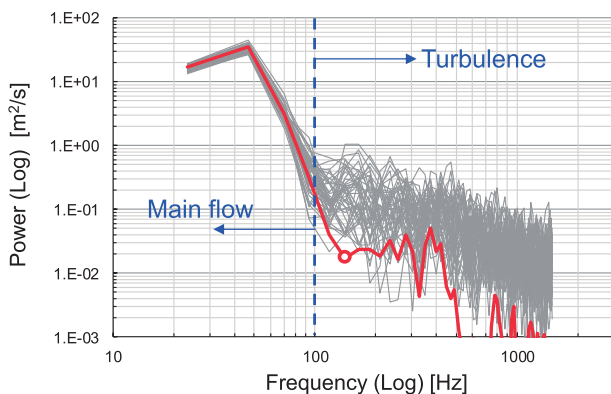
$$\tilde{u} = \langle u \rangle + u' + u_c \tag{1}$$

$$\tilde{u} = \bar{u} + u' \tag{2}$$

Many methods have been proposed for separating turbulent components from instantaneous flow velocity. The method used in this study was to use a cut-off frequency to separate between time-averaged components and turbulent components in the frequency domain[11][12]. This method has also been used by this author previously[2][13]. For frequency analysis, a fixed point in the central cross-section, just below the spark plug was used. Using a Fourier transformation on the velocity time-series data at this point, power spectra were obtained for every cycle (Fig. 5). The gray thin lines show the power spectra of the flow for one cycle each. The red thick line shows the power spectrum of the 45-cycles ensemble-averaged flow. Comparing the power spectra in Figure 5, it can be observed that all single cycle flows show power distributions very similar to the ensemble average up to about 100 Hz. Beyond this point, however the individual cycle's spectra deviate sharply from the ensemble-averaged, showing much higher power distribution compared to the ensemble-averaged between 100-1000 Hz. Therefore, it can be concluded that this

frequency range contains the turbulent component of the instantaneous flow. Thus, 100 Hz can be selected as the cutoff frequency.

This result differs from other literature referenced in this study. Kamimoto et al.[11] defined the cut-off frequency such that the non-turbulent component of the flow contained 90% of the accumulated power. This was done by integrating the power spectrum from left to right and choosing the frequency where the integral reached 90% of its total value. By this method, the cut-off frequency for the current data would be 400 Hz, which is significantly larger than the result of this study. It must be noted that Kamimoto et al. used the flow velocity during only the compression stroke to decide the cut-off frequency. On the other hand, in this study the cut-off frequency was decided based on the flow velocity in both the intake and compression strokes. As a result, a much higher range of velocity was considered in this study, which led to significant difference in cut-off frequency from the work of Kamimoto et al. Okura et al.[12] also decided the cut-off frequency using data from both intake and compression strokes. They defined the cut-off frequency as the frequency that exhibits the first minima of the power spectrum curve. Using this rule, the cut-off frequency for the current study would be 120Hz, as shown by red circle in Figure 5. This is almost the same as the result of this study. The cut-off frequency of 100 Hz adopted in this study was therefore judged to be appropriate when dealing with such a wide velocity range.

2-5. PLIF System

The intake system in Figure 3 is equipped with two injectors, a main injector at the port injection location and a sub injector placed further upstream to simulate uniform fuel distribution. These two injectors are same in terms of specifications. Since only the injector mounting positions are different, it is easy to obtain the same overall A/F ratio in both PFI and uniform conditions, and the flow pressure field is not affected. This helps reduce both errors due to unequal A/F and errors due to pressure dependence of the PLIF tracer. The fuel used in

Fig. 5 Power spectra of single cycle flows and ensemble average flow

this PLIF study was a mixture of 82% iso-octane and 18% 3-pentanone by volume. 3-pentanone is a widely used fluorescent tracer for PLIF measurements due to its strong fluorescence and low sensitivity to oxygen quenching. In addition, 3-pentanone has a boiling point of 101.5 degree C, which is quite similar to the boiling point of iso-octane (99 degree C),[14].

The fluorescence intensity is calibrated using the process shown in Figure 6. First, images are taken for several cycles with light sheet irradiation and without fuel injection. These images are ensemble-averaged to produce a background image. This background image is subtracted from the raw images during the 45 cycles. By doing so, the noise due to laser oscillation or optical defects is removed. Then, after cleaning and resetting the apparatus, another background image is acquired in a similar manner, and 45 cycles are performed using only the sub injector to produce a uniform fuel distribution. These 45 images are ensemble-averaged and then de-noised using the new background image. The resulting image represents the fluorescence intensity distribution of a homogenous stoichiometric mixture. Each de-noised PFI image is then divided by this homogenous distribution image to obtain the relative fuel concentration distribution. The final images therefore represent fuel concentration in one PFI cycle, normalized using the fluorescence intensity of the homogeneous stoichiometric mixture. To clarify, a value of 1 in the relative fuel

concentration images represents a stoichiometric mixture. Furthermore, since the fluorescence intensity and concentration of 3-pentanone are linear[14][15], the fuel concentration in the lean and rich regions does not require any further calibration.

Fluorescence of 3-pentanone excited at 266 nm shows dependence on pressure and temperature[16][17]. The measured in-cylinder pressure under PFI and uniform conditions are shown in Figure 7(a). Since the PFI condition and the uniform condition were set to the same load, the in-cylinder pressure was the same. Therefore, in the current case, pressure dependence of 3-pentanone can be ignored. The in-cylinder average temperature history is shown in Figure 7(b). This temperature was calculated using TPA (Three Pressure Analysis) model (GT-power ver7.3) from measured intake, exhaust and in-cylinder pressures. The in-cylinder temperature was different under PFI and uniform conditions. In PFI condition, fuel droplets evaporate more readily while suspended in the flow, since fuel is injected into the negative pressure field inside the intake port. On the other hand, in the uniform condition, fuel is injected into atmospheric pressure, so a large part of the evaporation occurs at the liquid wall film. The latent heat of vaporization from air is small, which leads to a higher in-cylinder temperature in the uniform condition. Figure 7(c) shows the temperature dependence of the fluorescence intensity of 3-pentanone referenced from Koch, Hanson, *et al*.[17]. Temperature correction was performed according to the calibration curve.
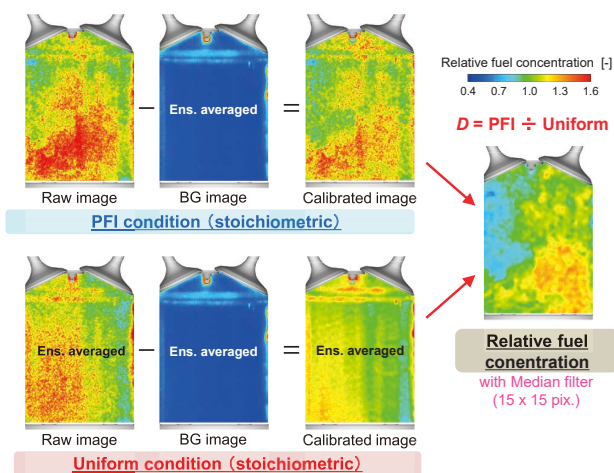
The fourth harmonic generation of Nd: YAG, used as the PLIF light source has a large shot-to-shot variation, so it is necessary to correct for laser intensity variation. In Figure 3, the part of the setup enclosed by red dashed lines is responsible for this correction. The light component transmitted through the HR266 nm mirror is photographed, and the correction coefficient is determined from the average luminance value of the image. The measured beam intensity fluctuation was approximately 9%, which is as per the catalog spec.

Fig. 6 Calibration process of fluorescence intensity

(a)

(b)

(c)
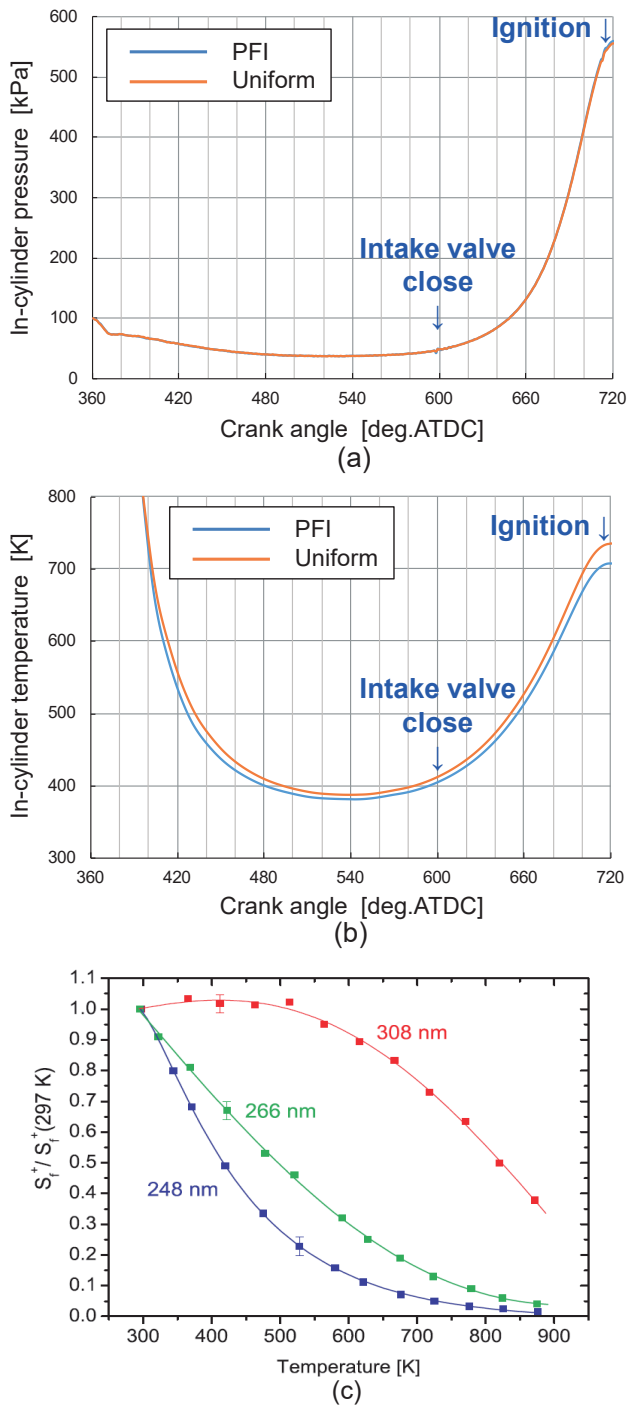
**Fig. 7 (a): Measurement result of in-cylinder pressure
(b): In-cylinder temperature estimated by 1-D simulation
(c): Temperature dependence of 3-pentanone[17]**

The relative fuel concentration D is expressed by the following equation (3)[15][18]:

$$D = C \frac{F_{PFI} - \langle B_{PFI} \rangle}{\langle F_{Uni} \rangle - \langle B_{Uni} \rangle} W_L c_{temp} \qquad (3)$$

where F_{PFI} is the individual image intensity of RAW image

in PFI condition, $\langle B_{PFI} \rangle$ is the ensemble-averaged image intensity of the background image obtained from the motored engine with light sheet and without fuel injection, $\langle F_{Uni} \rangle$ is the ensemble-averaged image intensity of the homogeneous fuel field in uniform condition, $\langle B_{Uni} \rangle$ is its ensemble average of background image for the uniform condition, W_L is correction factor of shot-to-shot variation of beam intensity, c_{temp} is correction factor of 3-pentanone's temperature dependence. It must be noted that F_{PFI} is the fluorescence intensity obtained under simultaneous measurement of PIV and PLIF, while $\langle F_{Uni} \rangle$ was obtained while performing only PLIF measurement. It was observed that when PIV and PLIF were measured simultaneously, the fluorescence intensity became higher than only PLIF measurement results. It is speculated that this is probably because the laser sheet thickness is increased by Mie scattering at 266 nm with the PIV tracer. The coefficient, C is introduced to correct the difference between simultaneous with PIV and only PLIF measurement.

2-6. Simultaneous Measurement of PIV and PLIF in Engine Firing Condition

Engine operating conditions are shown in the Table 3. The flow chart for the whole process of the measurements is shown in Figure 8. Warm-up is performed until the coolant temperature reached 70 degrees C with the engine stopped. After that, background images are acquired and simultaneous measurement of PIV and PLIF are performed in the order shown in Figure 8(a). The cylinder liner temperature increases rapidly during the firing operation. After 45 cycles of firing operation, the engine is stopped and cooled until the water temperature reaches approximately 30 degrees C. After sufficient cooling, the inside of the engine is cleaned. In order to minimize the influence of glass stains, the inside of the engine is cleaned after every firing operation. Next, a background image and a homogeneous pre-mixed gas image are taken as correction data (Fig. 8(b)).

The timing chart for the lasers and the cameras just before ignition are shown in Figure 9. The measurement timing just before ignition is 714 deg. for PIV and 713 deg. for PLIF. In the simultaneous measurement of PIV
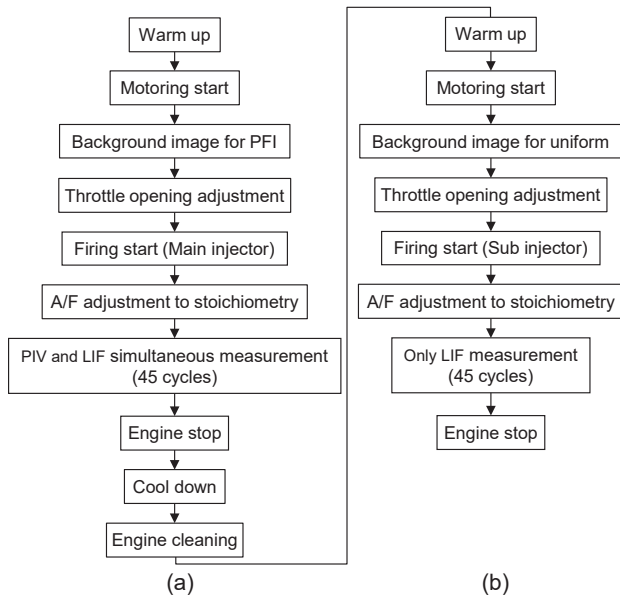
and PLIF, the two lasers are controlled to not operate at the same time. The fluorescence intensity detected by PLIF is weak compared to the scattered light intensity

detected by PIV. In order to measure the weak fluorescent light accurately, the oscillation timings of the two lasers are shifted.
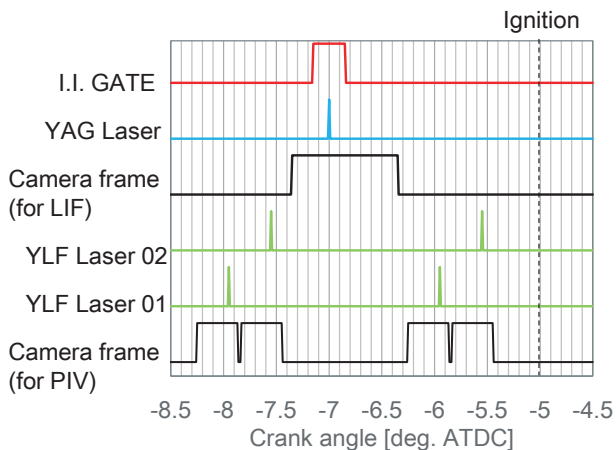
Table 3 Measurement conditions

Engine speed	1000 rpm
Minimum intake pressure (abs.)	37 kPa
Ignition timing	-5 deg. ATDC
Net IMEP (average)	150 kPa
CA50 (average)	50 deg. ATDC
Start of injection	180 deg. ATDC
Injection duration (average)	2.9 ms
A/F	Stoichiometric
Measurement cycles	45 cycles

(Fuel: iso-octane 82 vol. % + 3-pentanone 18 vol. %)

3 RESULTS AND DISCUSSION

3-1. Combustion Analysis for 45 Continuous Engine Cycles

Simultaneous measurement of TR-PIV and PLIF was performed under firing condition during 45 continuous cycles, and the cyclic fluctuation of the combustion was measured. The operating conditions are shown in Table 3. The results of the in-cylinder pressure history and the apparent heat release rate history are shown in Figure 10. The COV (Coefficient of Variation) of net IMEP in this measurement was 8.74%, which was equivalent to the COV measured while steady operation under the same
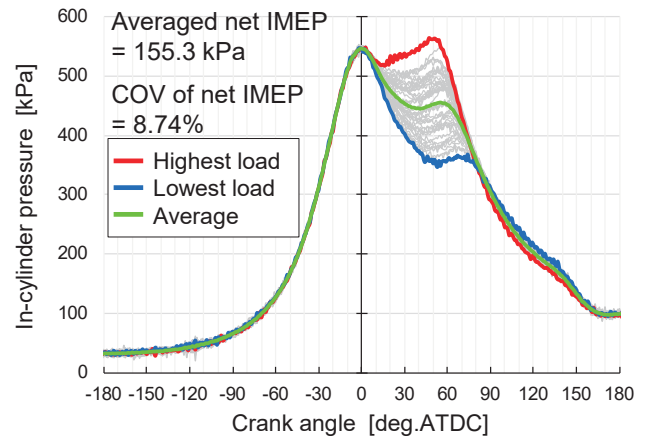
(a) In-cylinder pressure

(b) Apparent ROHR

Fig. 10 In-cylinder pressure and apparent rate of heat release during 45 cycles

(a)   (b)

Fig. 8 Measurement flow chart: (a) PFI condition (TR-PIV + PLIF) (b) Uniform mixture condition (PLIF only)
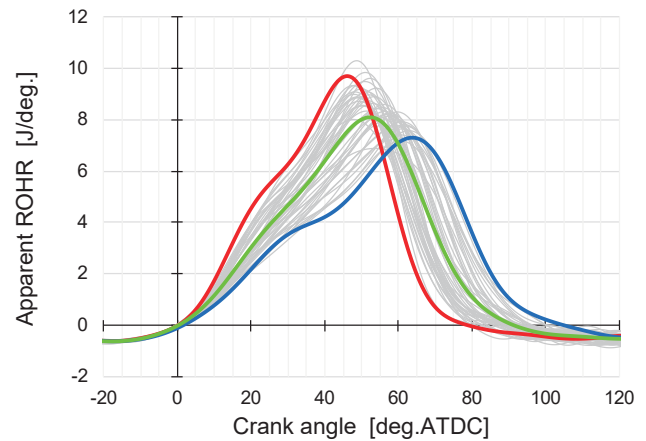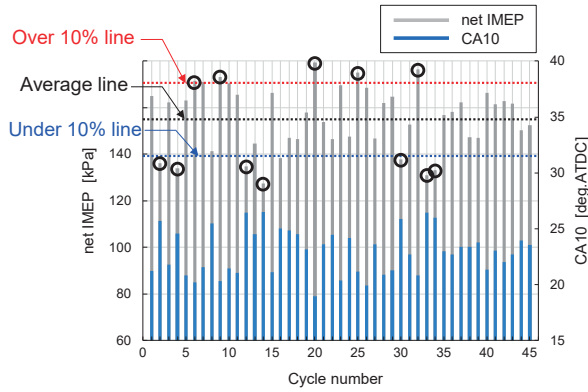

Fig. 9 Timing chart for TR-PIV and PLIF

Fig. 11 Individual cycle data on net IMEP and CA10

load with a metal sleeve. Figure 11 shows the net IMEP and CA10 for each cycle. In order to identify the factors affecting cyclic fluctuation in both high and low net IMEP cases, cycles with greater than 10% variation from mean net IMEP were extracted and analyzed. A total of 12 cycles were found to fit this criterion, out of which 5 were high work cycles and 7 were low work cycles. Although up to -20% variation has been reported in the past under similar load conditions, such a high variation was not observed in the 45 cycles analyzed in the current study.

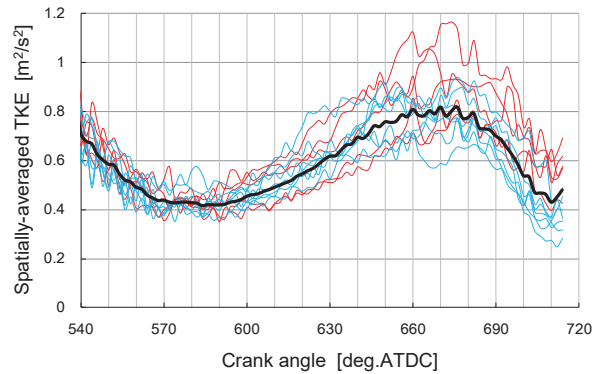## 3-2. Comparison of Kinetic Energy and Turbulence Kinetic Energy

Kinetic energy (KE) and turbulence kinetic energy (TKE) were obtained from the results of TR-PIV and the 12 cycles picked as mentioned were analyzed. Spatial averages of both kinetic energy and turbulence kinetic energy over the entire measurement area were calculated. Spatial averages were calculated for each crank angle using equation (4) and (5). In the equations, $\tilde{u}$ indicates instantaneous flow velocity, $\bar{u}$ indicates time averaged flow velocity, the subscripts, i, k indicate X, Z coordinates and the subscript, CA indicate crank angle. Note that equation (4) and (5) use time averages rather than ensemble averages as the mean value. Therefore, KE and TKE are the values for one cycle only.

$$KE_{(CA)} = \frac{1}{N_x N_z} \sum_{i=1}^{N_x} \sum_{k=1}^{N_z} \frac{1}{2}\left(\bar{u}_{(i,k,CA)}^2 + \bar{w}_{(i,k,CA)}^2\right) \qquad (4)$$

$$TKE_{(CA)} = \frac{1}{N_x N_z} \sum_{i=1}^{N_x} \sum_{k=1}^{N_z} \frac{1}{2}\left\{\left(\tilde{u}_{(i,k,CA)} - \bar{u}_{(i,k,CA)}\right)^2 + \left(\tilde{w}_{(i,k,CA)} - \bar{w}_{(i,k,CA)}\right)^2\right\}$$
$$(5)$$
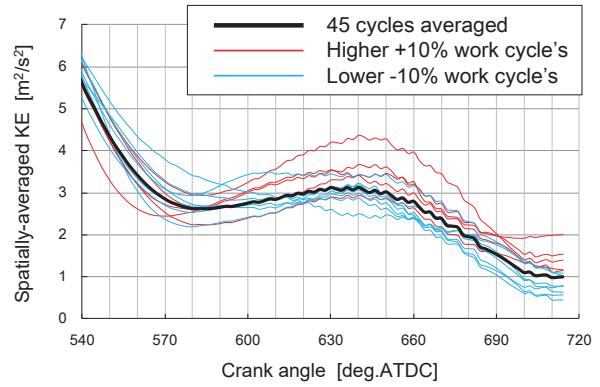
(a) Spatially-averaged kinetic energy

(b) Spatially-averaged turbulent kinetic energy

Fig. 12 Spatially-averaged kinetic energy and turbulence kinetic energy

Figure 12 shows the spatially-averaged history of KE and TKE. The black thick line in the figure is the average value of 45 cycles. Blue thin lines indicate the 7 cycles with low net IMEP, while red thin lines indicate the 5 cycles with high net IMEP. From the KE history shown in Figure 12(a), a correlation between net IMEP and KE cannot be confirmed up to around CA = 600 deg. ATDC. However, from CA = 660 deg. ATDC onwards, the high net IMEP cycles (red lines) exceed the average value and the low net IMEP cycles (blue lines) are consistently below the average value. This correlation is especially clear at the right end of the graph (CA = 714 deg. ATDC), just before ignition timing. It is therefore, reasonable to infer that high net IMEP cycles show high KE, and that the converse holds for low net IMEP cycles. A similar trend is observed for TKE (Fig. 12(b)), with high net IMEP cycles showing higher than average TKE and low IMEP cycles showing lower than average values for crank angles after ~660 deg. ATDC. However, two out of the 12 cycles do not strictly follow the aforementioned
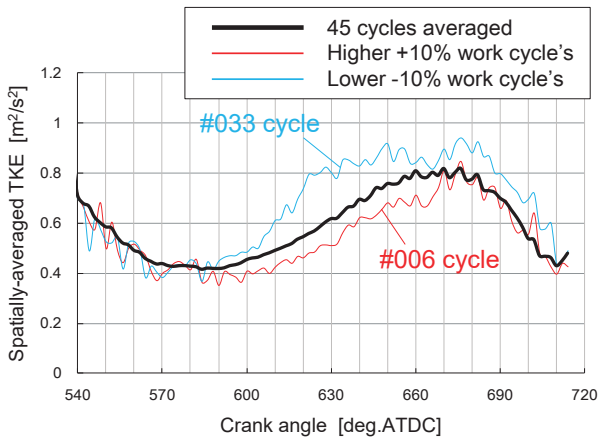
Fig. 13 Two irregular cycles on TKE

(a) Averaged-flow (b) Distribution of TKE (c) Distribution of relative fuel concentration

Fig. 14 Average flow pattern, distributions of TKE and fuel concentration at 714 deg. ATDC in low work cycle

(a) Averaged-flow (b) Distribution of TKE (c) Distribution of relative fuel concentration

Fig. 15 Average flow pattern, distributions of TKE and equivalence ratio at 714 deg. ATDC in high work cycle

correlation. As shown in Figure 13, the # 033 cycle, despite being a low net IMEP case, shows higher than average TKE. On the other hand, cycle # 006 has high net IMEP but its TKE is similar to the average value. For these two cycles, it is possible that factors other than TKE have a stronger influence on net IMEP. Therefore, in order to analyze these cases further, the time-averaged flow distribution, TKE distribution and fuel concentration distribution at just before ignition timing are also compared.

3-3. Comparison of Spatial Distribution Just Before Ignition

Figures 14 and 15 show the time-averaged flow and TKE distribution 1 degree before ignition timing, and the relative fuel concentration distribution 2 degrees before ignition timing respectively. From left to right the figure shows the time-averaged flow pattern, TKE distribution, and relative fuel concentration distribution. In Figure 14, the 7 low work cycles are arranged from top to bottom in ascending order of net IMEP. In Figure 15, the 5 high work cycles are arranged in a similar order. Comparing the time-averaged flow patterns in Figures 14 and 15, the difference in the tumble vortex is the most notable feature. In high work cycles, a strong upward tumble flow can be observed close to the spark plug in the right half of the cross section. However, in low work cycles, this flow is generally weaker and farther away from the spark plug.
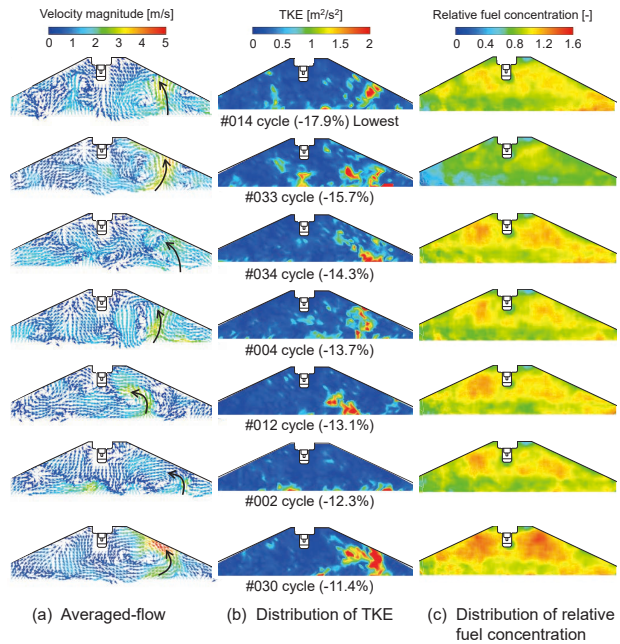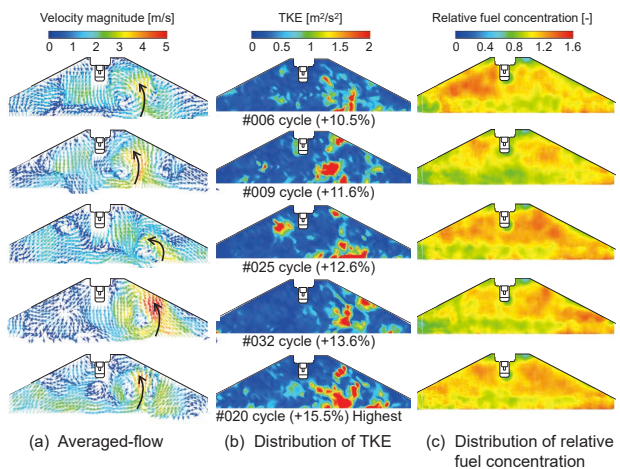
Comparing TKE distribution, it can be seen that the high work cycles generally have higher TKE throughout the cross section compared to low work cycles. Furthermore, in high work cycles, regions of very high TKE exist close to the spark plug. The exceptions to this rule is the low work cycle # 033, where a high TKE distribution can be observed under the spark plug, and the TKE appears to be relatively high as a whole. This agrees with the result of TKE spatial average shown in Figure 13.

Comparing the relative fuel concentration distribution, all the results appear similar. In the case of PFI exhaust stroke injection, the fuel is almost uniformly distributed at the ignition timing. Unlike in DI conditions[7], any localized variation of fuel distribution that could cause significant cyclic fluctuation cannot be identified. Focusing on the # 033 cycle in Figure 14, it can be seen that the relative fuel concentration is clearly leaner than all other cycles. As discussed above (Fig. 12, 13), # 033 cycle does not conform to the apparent relation between net IMEP and TKE, showing higher than average TKE despite having low net IMEP. In this cycle, it is assumed that low fuel concentration is the reason for the net IMEP being below average. On the other hand, looking at the # 006 cycle in Figure 15, it can be seen that the relative fuel concentration is one of the highest among all cycles. As discussed above, net IMEP in cycle # 006 should be low because the TKE is low. However, it appears that the rich mixture compensates for the low TKE, resulting in a high net IMEP.

Therefore, considering from the above results, a clear correlation has been established between TKE and net IMEP for 10 of the 12 (about 80%) cycles analyzed. In the remaining 2 cycles (about 20%), it is found that the fuel concentration just before ignition timing has a greater effect on net IMEP than TKE.

3-4. Contribution of TKE and fuel concentration to combustion fluctuation

In previous section, relatively low and high net IMEP cycles have been explained with TKE and fuel concentration of each cycles. In this section, the contribution of the two physical properties are analyzed. A dataset of another 45 cycles measured under the same conditions is added, and analysis is performed using data from a total of 90 cycles.

Figure 16(a) shows a scatter plot of the net IMEP for all 90 cycles. The contours show normalized net IMEP, and the 12 cycles analyzed above are marked with triangles (yellow triangle: high work cycle, purple triangle: low work cycle). The horizontal axis is the normalized relative
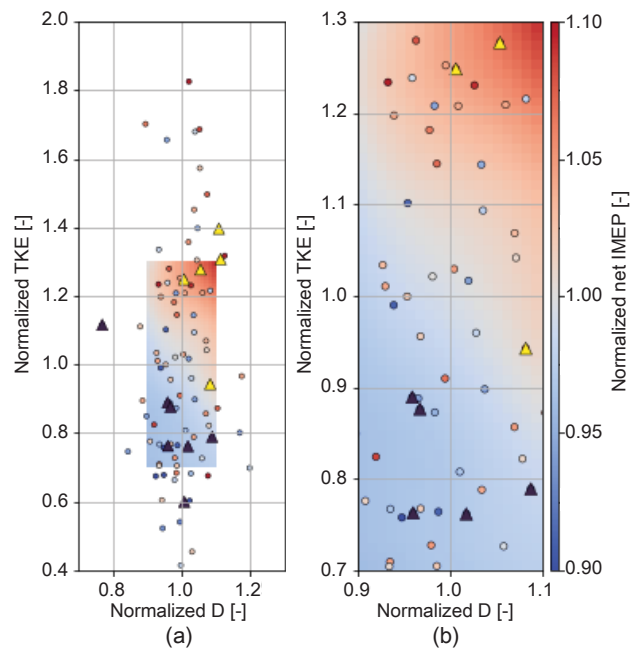

Fig. 16 Scatter plot and response surface: (a) A region containing all 90 data (b) A region with densely populated data (48 of 90 data)

fuel concentration D, and the vertical axis is normalized TKE. A response surface was calculated from this data by smoothing with RBF (Radial basis function) interpolation. RBF interpolation was calculated using the Python library (Python 3.7.2, ScyPy 1.2.1). The response surface within the range $D = 0.9$ to 1.1 and TKE = 0.7 to 1.3 is shown in Figure 16(a). This range contains 48 of the total 90 data points, and the density of the data is relatively high. Due to the nature of RBF interpolation, the response surface may not be sufficiently accurate in regions where data is sparse. Thus the response surface calculation is limited only to this region with densely populated data. Figure 16(b) shows a zoomed-in image of only the response surface area.

Figure 17 shows the error between the response surface prediction and the actual measurement value. The solid line indicates the mean value (μ) of the error, and the dashed line indicates the standard deviation (σ). The error of the response surface is within $\pm 15\%$, and the standard deviation is about 7%.
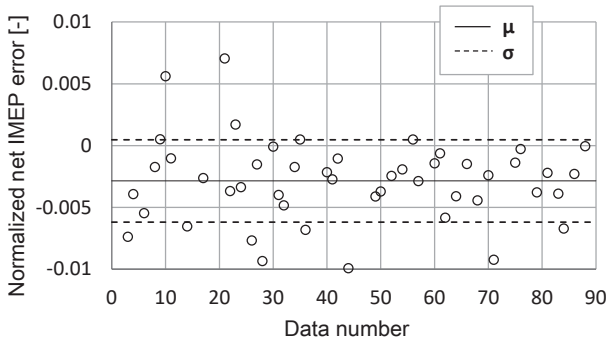
Figure 18 shows the plots for net IMEP vs. TKE at $D = 1$, and net IMEP vs. D at TKE = 1. From the net IMEP vs. D
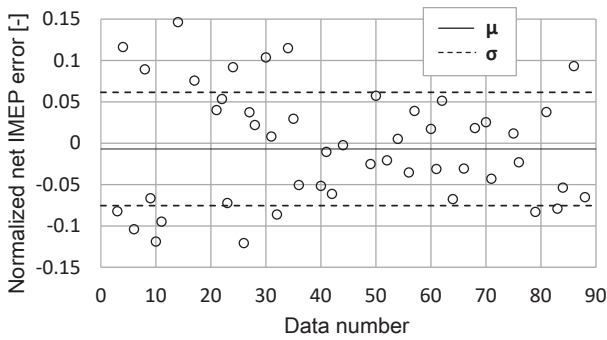
Fig. 17 Error between the response surface prediction
and the actual measurement value.
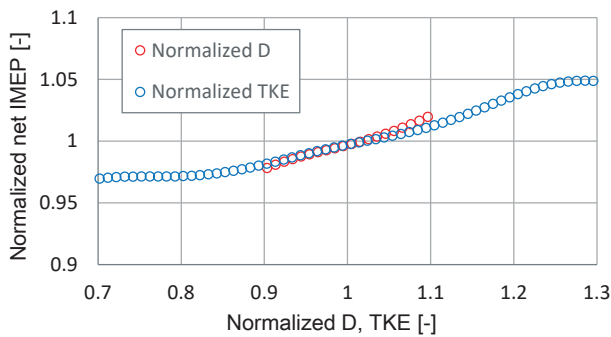
Fig. 18 Plots for net IMEP vs. TKE at $D = 1$,
and net IMEP vs. D at TKE = 1

Fig. 19 Error between the approximate response surface
equation and the RBF response surface prediction value.

graph, net IMEP was expressed as a polynomial of D. Similarly, from the plot of TKE and net IMEP, net IMEP was expressed as a polynomial of TKE. The product of these two polynomials was taken to create an approximation of the net IMEP response surface.

$$netIMEP_{norm} = \sum_{k=0}^{n} a_k D_{norm}{}^k \sum_{k=0}^{n} b_k TKE_{norm}{}^k \qquad (6)$$

In the equation (6), the subscript, norm means a value normalized by ensemble average value. Figure 19 shows

the error in this approximate response surface compared to the response surface obtained using RBF interpolation. The error in the approximate response surface is within $\pm 1\%$ of the RBF surface, and the standard deviation is approximately 0.3%. Thus, the approximate response surface equation and the response surface obtained using RBF interpolation are almost equal.

As can be seen from Figure 18, the slopes of net IMEP with respect to fuel concentration D and TKE are almost equal in the area where data is densely populated. This indicates that the sensitivity of net IMEP to D and TKE is almost the same in this region. The standard deviation of TKE for all 90 data points is approximately 0.31, and the same for D is approximately 0.07. Since the overall variation in TKE is about 4 times larger than the variation in D, it can be concluded that the fluctuation of TKE is responsible the fluctuation in net IMEP in most cases in this measurement.

3-5. Factors Affecting TKE Fluctuation at Ignition Timing

The previous section shows that most of the combustion fluctuation is caused by TKE fluctuation in this study. In order to realize an engine with minimal CCV, it is necessary to clarify the mechanism of TKE fluctuation. In this section, the characteristics of time-averaged flow are analyzed for cycles with large combustion fluctuations.

Time-averaged flow was compared for the cycles with maximum and minimum net IMEP. Figures 20 and 21 show the vector maps of the time-averaged flow from CA 420 deg. to 660 deg. in intervals of 30 degrees and vector maps of the time-averaged flow just before ignition. It must be noted that the color scale of the flow velocity is different for the intake strokes, compression strokes and just before ignition. Velocity magnitude ranges from 0 to 25 m/s in the intake stroke, 0 to 7 m/s in the compression stroke and 0 to 5 m/s at just before ignition. Figure 20 shows the time-averaged flow pattern of the maximum work cycle (# 020), and Figure 21 the minimum work cycle (# 014). Comparing the two time-averaged flows, it can be observed that significant
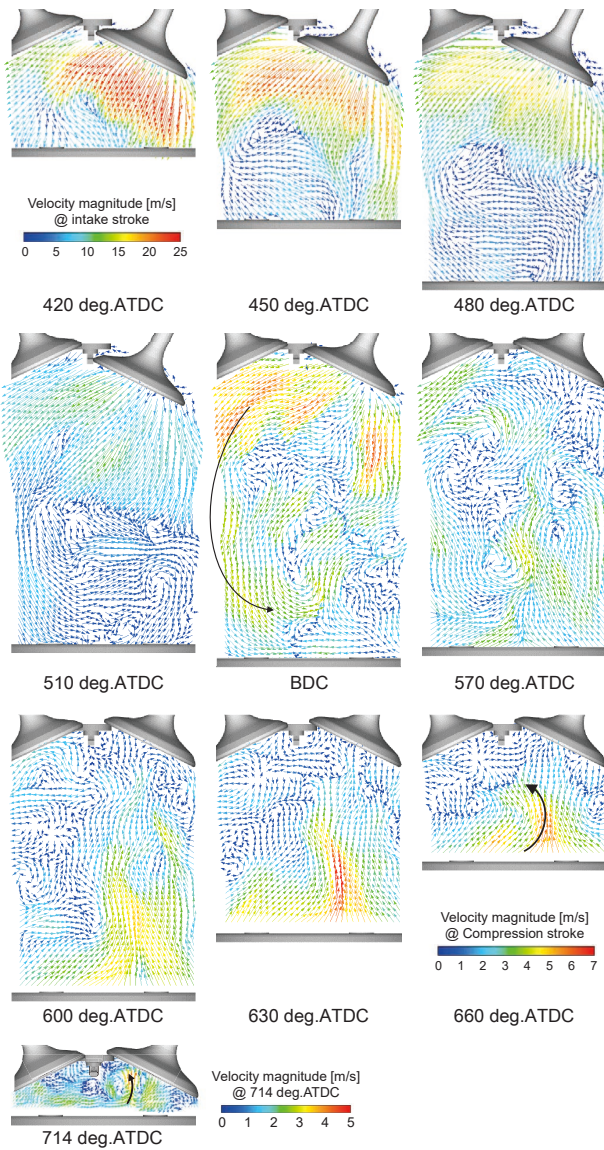
Velocity magnitude [m/s] @ intake stroke
0 5 10 15 20 25

420 deg.ATDC   450 deg.ATDC   480 deg.ATDC

510 deg.ATDC   BDC   570 deg.ATDC

600 deg.ATDC   630 deg.ATDC   660 deg.ATDC

Velocity magnitude [m/s] @ Compression stroke
0 1 2 3 4 5 6 7

714 deg.ATDC

Velocity magnitude [m/s] @ 714 deg.ATDC
0 1 2 3 4 5

Fig. 20 Time-averaged flow patterns in the highest work cycle (# 020)

Velocity magnitude [m/s] @ intake stroke
0 5 10 15 20 25

420 deg.ATDC   450 deg.ATDC   480 deg.ATDC

510 deg.ATDC   BDC   570 deg.ATDC

600 deg.ATDC   630 deg.ATDC   660 deg.ATDC

Velocity magnitude [m/s] @ Compression stroke
0 1 2 3 4 5 6 7

714 deg.ATDC

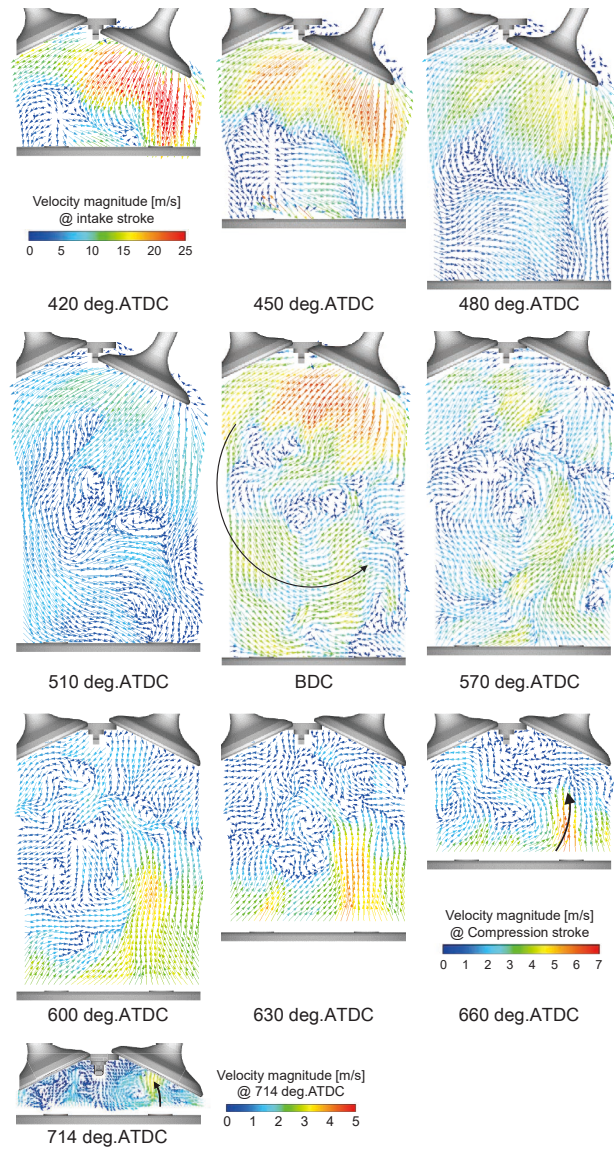**Velocity magnitude [m/s] @ 714 deg.ATDC**
0 1 2 3 4 5

Fig. 21 Time-averaged flow patterns in the lowest work cycle (# 014)

difference exists in the direction and size of the tumble vortex during the intake stroke, as highlighted by black arrows at BDC (bottom dead center) in either figure. For the maximum work cycle, the flow entering from the top of the intake valve rotates counter-clockwise in a wide arc, contacting the piston crown near the center of the bore. On the other hand, in the minimum work cycle, this flow appears to follow a tighter arc, and is nearly parallel to the piston surface near the center of the bore. This difference is likely due to the horizontal offset of the large scale tumble vortex structure during the intake stroke. A schematic diagram of this horizontal offset is shown in Figure 22. In this figure, the red arrow
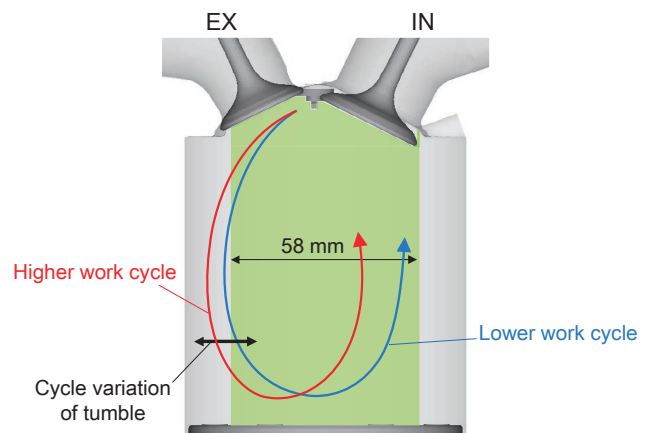

EX   IN

58 mm

Higher work cycle

Lower work cycle

Cycle variation of tumble

Fig. 22 Schematic drawing of horizontal offset of tumble flow structure

indicates a high work cycle, the blue arrow indicates a low work cycle, and the region highlighted in green represents the TR-PIV measurement range. It can be seen from this schematic that the tumble flow in the higher work cycle is offset to the left and approaches the piston crown at a downward angle, while the same flow in the low work cycle is offset to the right and is almost horizontal as it approaches the piston crown at the center of the bore. Focusing within the measurement range, this vortex structure is consistent with the flow patterns of Figures 20 and 21. Moving further to the compression stroke, another noticeable difference is apparent in these two cases. The flow patterns on the piston crown surface after BDC are compared in Figure 20 and Figure 21. As indicated by the black arrow at CA = 660 deg. ATDC in either figure, it can be seen that a strong upward flow is formed near the spark plug in the maximum work cycle. On the other hand, in the minimum work cycle, this upward flow is farther from the plug towards the right and the flow velocity is relatively lower. This upward flow remains until the ignition timing, resulting in a strong average flow near the plug just before ignition in the

maximum work cycle. On the other hand, in the minimum work cycle, this upward flow is at a position farther away from the plug, and a weak average flow is distributed near the spark plug just before ignition. Furthermore, as discussed before and shown in figures 14 and 15, patches of high TKE are distributed near the plug in the maximum work cycle (# 020), whereas TKE distribution near the plug in the minimum work cycle (# 014) is generally lower. Thus, it can be confirmed that the cyclic fluctuation of the tumble vortex structure during intake stroke has a significant effect on the fluctuation of the flow and TKE distribution at ignition timing.

In order to obtain further confirmation of the
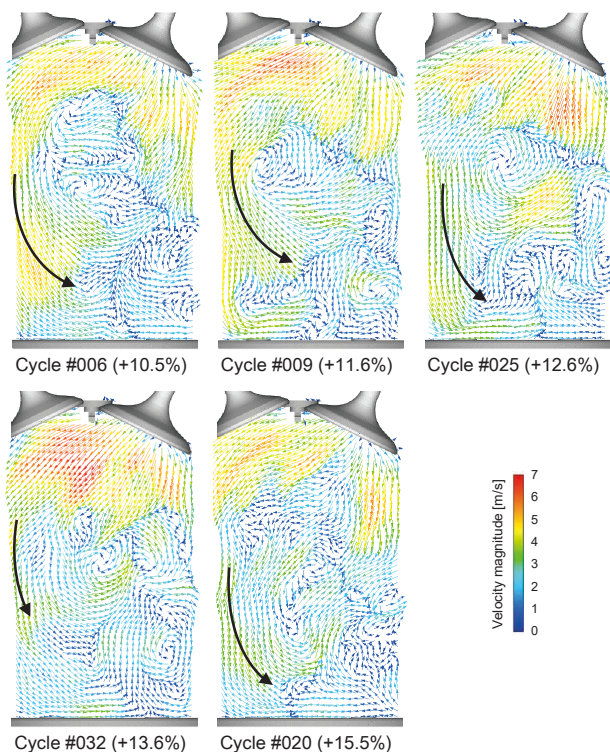
Fig. 23 Flow patterns at BDC in the case of the higher work cycles
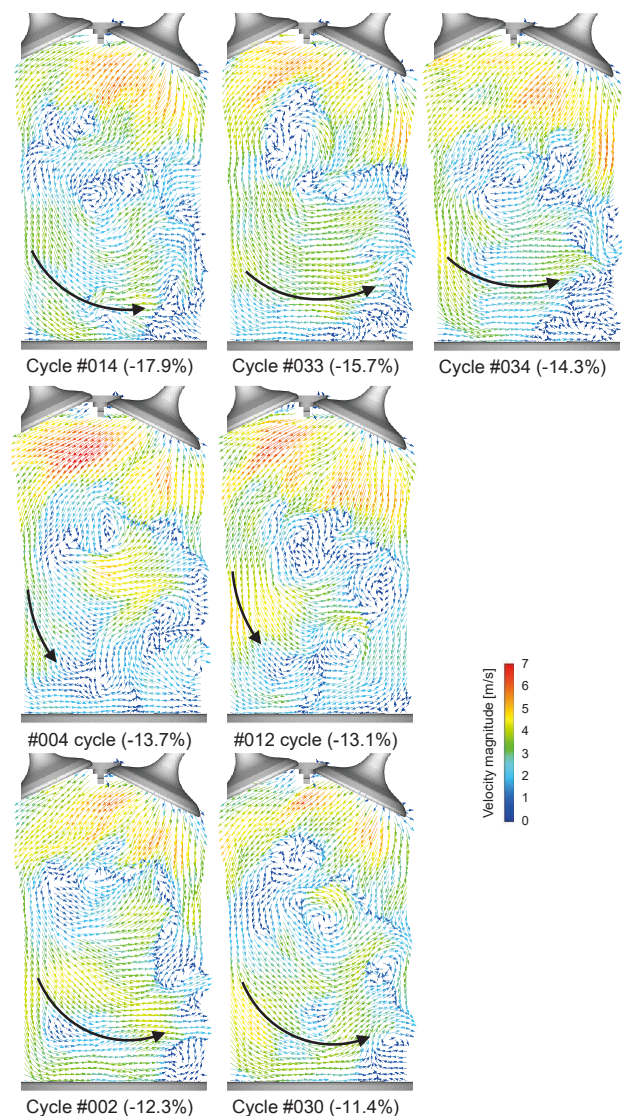
Fig. 24 Flow patterns at BDC in the case of the lower work cycles

aforementioned tumble vortex offset, time-averaged flow patterns at BDC were compared for all 12 shortlisted cycles with high variation from mean IMEP. Figure 23 shows the time-averaged flow patterns at BDC for the 5 higher work cycles, and Figure 24 shows that of the 7 lower work cycles. For the high work cycles shown in Figure 23, it can be seen that the tip of the tumble flow is at or to the left of the center of the bore as indicated by the black arrows. On the other hand, for the lower work cycles shown in Figure 24, five out of 7 cycles have a flow feature supporting the aforementioned tumble vortex offset. In these 5 cycles (# 014, # 033, # 034, # 002, # 030), it can be seen that the tumble tip is on the right side of the bore center and the flow direction itself is almost horizontal near the center. Therefore, the correlation between tumble vortex offset and net IMEP holds true not only for the two extrema cycles, but also for the most of high variation cycles analyzed in this study.

4　SUMMARY

In this study, simultaneous measurement of TR-PIV and PLIF was conducted to analyze the influence of flow and fuel concentration fluctuations on CCV of combustion.

Out of 45 cycles measured successively under continuous engine firing, analysis was performed on 12 cycles which have big difference of net IMEP from the average. It has been confirmed that the cycle-to-cycle variation of combustion can be connected to the fluctuation of TKE and relative fuel concentration at the ignition timing. It has been also observed that the number of cycles showing high combustion fluctuation due to TKE variation was significantly greater than the number of cycles showing fluctuation due to fuel concentration.

From 90 cycle data, a response surface of net IMEP on two parameters, fuel concentration and TKE, was calculated by smoothing with RBF interpolation. The response surface shows about 7% standard deviation from the experimental results. From the characteristics of this response surface, it is judged that net IMEP is almost equally sensitive to variations in both fuel concentration and TKE. Furthermore, by comparing the relative variation of fuel concentration and TKE, it has been confirmed that TKE variation is the primary cause of cyclic fluctuation in a majority of the cases measured in this study. This is likely due to the fact that in a PFI engine, variations in fuel concentration are usually not very high.

As in the previous author's study, it has been confirmed that the fluctuation of TKE at the ignition timing is affected by the tumble vortex structure during the intake stroke. In the future, it could be worthwhile to further investigate and elucidate the mechanism by which the tumble vortex structure changes during the intake stroke.

REFERENCES

[1] Müller, R. H. S., Böhm, B., Gleißner, M., Grzeszik. R., Arndt, S. and Dreizler, A., Flow field measurement in an optically accessible, direct-injection spray-guided internal combustion engine using high-speed PIV, Experimental Fluids, Vol. 48, Issue 2 (2010), pp.281-290.

[2] Hokimoto, S., Kuboyama, T., Moriyoshi, Y., Iida, M. and Watanabe, T., Analyses of cycle-to-cycle variation of combustion and in-cylinder flow in a port injection gasoline engine using PIV and PLIF techniques, SAE technical paper (2017), 2017-01-2213.

[3] Sholes, R. K., Kawashima, J. and Mori, S., Analysis of in-cylinder gas flow and its cyclic variability using PIV, Transactions of the Society of Automotive Engineers of Japan, Vol.36, No.6 (2005), pp.25-30 (in Japanese).

[4] Zeng, W., Sjoberg, M. and Reuss, D., Using PIV measurements to determine the role of the in-cylinder flow field for stratified DISI engine combustion, SAE International Journal of Engines, Vol.7, No.2 (2014), pp.615-632, doi:10.4271/2014-01-1237.

[5] Fontanesi, S., d'Adamo, A. and Rutland, J. C., Large-eddy simulation analysis of spark configuration effect on cycle-to-cycle variability of combustion and knock, International Journal of Engine Research, Vol.16, Issue 3 (2015), pp.403-418.

[6] Peterson, B., Reuss, L. D. and Sick, V., High-speed

imaging analysis of misfires in a spray-guided direct injection engine, Proceedings on the Combustion Institute, Vol.33, No.2 (2011), pp.3089-3096.

[7] Peterson, B., Reuss, L. D. and Sick, V., On the ignition and flame development in a spray-guided direct-injection spark-ignition engine, Combustion and Flame, Vol.161, No.1 (2014), pp.240-255.

[8] The Visualization Society of Japan, PIV Handbook, The first edition issued 4th Printing (2013), Morikita Publishing Co., Ltd (in Japanese).

[9] Keane, D. R. and Adrian, J. R., Optimization of particle image velocimeters: II multiple pulsed systems, Measurement Science and Technology, Vol.2 (1991), pp.963-974.

[10] The Visualization Society of Japan, The 20th Visualization frontier "Training session of PIV 2015 (Osaka)" (2015) (in Japanese).

[11] Kamimoto, T., Yagita, M., Moriyoshi, Y., Kobayashi, N. and Morita, H., An experimental study of in-cylinder air flow with a transparent cylinder engine, Transactions of the Japan Society of Mechanical Engineers, Series B, Vol.53, No.492 (1987), pp.2686-2693 (in Japanese).

[12] Okura, Y., Higuchi, K., Urata, Y., Someya, S. and Tanahashi, M., Measurement of in-cylinder turbulence in an internal combustion engine using high speed particle image velocimetry, Transactions of the Japan Society of Mechanical Engineers, Series B, Vol.79, No.806 (2013), pp.319-332 (in Japanese).

[13] Hokimoto, S., Kuboyama, T., Moriyoshi, Y., Haramiishi, S., Watanabe, T. and Iida, M., Analyses of cycle-to-cycle variation of combustion at low load condition by using high-speed PIV and direct photographing of early flame propagation, Transactions of the Japan Society of Mechanical Engineers, Series B, Vol.84, No.865 (2018), pp.18-00051 (in Japanese).

[14] Fujikawa, T., Hattori, Y. and Akihama, K., "Quantitative 2-D Fuel Distribution Measurements in as SI Engine Using Laser-Induced Fluorescence with Suitable Combination of Fluorescence Tracer and Excitation Wavelength", SAE Technical Paper 972944, 1997, doi:10.4271/972944.

[15] Fujikawa, T., Hattori, Y., Koike, M., Akihama, K., Kobayashi, T. and Matsushita, S., "Quantitave 2-D Fuel Distribution Measurements in a Direct-Injection Gasoline Engine Using Laser-Induced Fluorescence Technique", JSME International Journal, Series B, Vol.42, No.4, pp.760-767, 1999.

[16] Modica, V., Morin, C. and Guibert, P., "3 - Pentanone PLIF at elevated temperatures and pressure: measurements and modeling", Journal of Applied Physics B, Vol. 87, Issue 1, pp.193-204, 2007.

[17] Koch, D. J. and Hanson, K. R., "Temperature and excitation wavelength dependencies of 3-pentanone absorption and fluorescence for PLIF applications", Journal of Applied Physics B, Vol.76, Issue 3, pp.319-324, 2003.

[18] Kim, S., Yan, Y., Nouri, M. J. and Arcoumanis, C., "Effects of intake flow and coolant temperature on the spatial fuel distribution in a direct-injection gasoline engine by PLIF technique", Fuel, Vol.106, pp.737-748, 2013.

DEFINITIONS/ABBREVIATIONS

CCV	Cycle-to-cycle variation
PFI	Port fuel injection
DI	Direct injection
TR-PIV	Time resolved particle image velocimetry
PLIF	Planer laser induced fluorescence
HR	High reflection
HT	High transmission
Δt	Interval between two laser shots
ATDC	After top dead center
COV	Coefficient of variation
I. I.	Image intensifier
net IMEP	Net indicated mean effective pressure
CA10,(CA50)	Timing at 10% (50%) of accumulated heat release
FFT	Fast Fourier transform
KE	Kinetic energy
TKE	Turbulence kinetic energy
BDC	Bottom dead center

■著者

孕石 三太
Santa Haramiishi
技術・研究本部
研究開発統括部
先進システム開発部

渡辺 敬弘
Takahiro Watanabe
技術・研究本部
FSR 開発部

飯田 実
Minoru Iida
技術・研究本部
研究開発統括部

保木本 聖
Satoshi Hokimoto
サステナブル・エンジン・
リサーチセンター
研究員

窪山 達也
Tatsuya Kuboyama
千葉大学大学院
工学研究院 機械工学コース
次世代モビリティパワーソース
研究センター 准教授

森吉 泰生
Yasuo Moriyoshi
千葉大学大学院
工学研究院 機械工学コース
次世代モビリティパワーソース
研究センター長・教授